

Uncertainty and Sensitivity Analysis of Afterbody Radiative Heating Predictions for Earth Entry

Thomas K. West IV* and Christopher O. Johnston†

NASA Langley Research Center, Hampton, VA 23681

Serhat Hosder‡

Missouri University of Science and Technology, Rolla, MO 65409

The objective of this work was to perform sensitivity analysis and uncertainty quantification for afterbody radiative heating predictions of Stardust capsule during Earth entry at peak afterbody radiation conditions. The radiation environment in the afterbody region poses significant challenges for accurate uncertainty quantification and sensitivity analysis due to the complexity of the flow physics, computational cost, and large number of uncertain variables. In this study, first a sparse collocation non-intrusive polynomial chaos approach along with global non-linear sensitivity analysis was used to identify the most significant uncertain variables and reduce the dimensions of the stochastic problem. Then, a total order stochastic expansion was constructed over only the important parameters for an efficient and accurate estimate of the uncertainty in radiation. Based on previous work, 388 uncertain parameters were considered in the radiation model, which came from the thermodynamics, flow field chemistry, and radiation modeling. The sensitivity analysis showed that only four of these variables contributed significantly to afterbody radiation uncertainty, accounting for almost 95% of the uncertainty. These included the electronic-impact excitation rate for N between level 2 and level 5 and rates of three chemical reactions influencing N, N⁺, O, and O⁺ number densities in the flow field.

Nomenclature

D	Statistical variance	T_v	Vibrational-Electronic Temperature
I	Intensity	x	Deterministic Variable
N_s	Number of Samples	α	Deterministic Coefficient in the Polynomial Chaos Expansion
N_t	Number of Terms in a Total-Order Polynomial Chaos Expansion	α^*	Random Function
n	Number of Random Dimensions	δ	Truncation Error
P	Pressure	Ψ	Random Basis Function
p	Order of Polynomial Expansion	μ_e	Mean Error
S_e	Absolute Error	ξ	Standard Input Random Variable
S_T	Total Sobol Index		

I. Introduction

During high-speed Earth entry, radiation can significantly affect surface heating of an entry vehicle. Lunar and planetary return missions may experience entry conditions that generate significant shock-layer radiation. Radiating species may expand from the forebody into the afterbody region, which may cause substantial radiative heating on the afterbody surfaces. Previous work by Johnston and Brandis¹ showed the importance of afterbody radiative heating. Because of complex modeling associated with quantifying

*Aerospace Engineer, Vehicle Analysis Branch, Systems Analysis and Concepts Directorate, Member AIAA.

†Aerospace Engineer, Aerothermodynamics Branch, Research Directorate, Member AIAA.

‡Associate Professor of Aerospace Engineering, Department of Aerospace and Mechanical Engineering, Senior Member AIAA.

the radiation in the afterbody, a large amount of uncertainty exists, which can drastically affect radiative heating predictions. Johnston and Brandis¹ stated that there was a definite need for an uncertainty and sensitivity analysis to help inform resource allocation for improved modeling and experimental testing. This previous study laid the ground work for afterbody radiation modeling and, therefore, is the foundation of the current work.

The primary objective of this work is to investigate the uncertainty in high-fidelity radiative heat flux predictions on the afterbody of the Stardust sample return capsule geometry during Earth entry. The high-fidelity computational fluid dynamics (CFD) model is composed of the LAURA² thermochemical nonequilibrium flow solver coupled with the nonequilibrium radiation code, HARA.^{3,4} A full ray-tracing model is implemented for improved radiation prediction on the vehicle surface. Additionally, forebody ablation is modeled to account for the impact of ablation products that have expanded into the afterbody region. Johnston and Kleb⁵ performed a detailed uncertainty analysis of forebody radiative heating during Lunar-return Earth entry. Similar uncertainty sources in the computational model are considered in the present study, which include flow field chemical rate models, atomic line emission and absorption, photoionization cross-sections, the two-temperature model, negative ion cross-sections, molecular band oscillator strengths, and the excitation/deexcitation rates of molecular electronic states. Additionally, a global nonlinear sensitivity analysis is performed to identify key parameters that contribute significantly to the to uncertainty.

Due to the complexity and significant computational cost of the numerical simulations of planetary entry flows, performing uncertainty quantification (UQ) with traditional sampling approaches (i.e., Monte Carlo) may not be feasible. Following the approach by West and Hosder,⁶ the objective will be to implement a surrogate modeling approach to replace the computationally expensive deterministic model during uncertainty propagation. This process is based on constructing a stochastic expansion through the use of a sparse approximation of the point-collocation nonintrusive polynomial chaos (NIPC) method. The goal is to minimize the number of computationally expensive deterministic model evaluations needed for an accurate UQ analysis. The approximation is calculated iteratively by increasing the number of CFD evaluations until a converged surrogate model is obtained.

The impact of this work is primarily the sensitivity analysis of various parameters in the afterbody radiation modeling and quantifying the amount of uncertainty in backshell radiative heating expected for high speed (greater than 10 km/s) Earth entry. In the near term, with the upcoming Orion flight to the moon and back, this information is critical to ensuring that the thermal protection is reliable and robust to protect future crews. Future sample and Mars return missions will also experience similar conditions during entry and this information will be valuable for vehicle design. Additionally, the resulting sensitivity analysis can be important for future work to allocate resources for improving the accuracy of computational models and reducing epistemic uncertainty.

The following section briefly describes the types of uncertainty in computational modeling. Section III outlines the surrogate modeling approach using NIPC with a sparse approximation. Section IV describes the baseline radiative heating model for the Stardust sample return capsule entry scenario. Details regarding the CFD model, entry conditions, and discussion of baseline solution are also given in this section. Section V presents the results and discusses important conclusions.

II. Types of Uncertainty in Numerical Models

A critical step in any uncertainty analysis is the classification of the uncertain parameters. These parameters may be mathematically represented differently based on the nature of their uncertainty. Incorrect classification and/or treatment of uncertain parameters can result in widely varying output uncertainty.

Two main types of uncertainty exist in numerical modeling: aleatory uncertainty and epistemic uncertainty.⁷ Aleatory uncertainty is the inherent variation of a physical system. Such variation is due to the random nature of input data and can be mathematically represented by a probability density function if substantial experimental data is available for estimating the distribution type. An example of this type of uncertainty could be the fluctuations in freestream quantities. While still considered random variables, these variations are not controllable and are sometimes referred to as irreducible uncertainties.

Epistemic uncertainty in a stochastic problem comes from several potential sources. These include a lack of knowledge or incomplete information of the behavior of a particular variable. Also, ignorance or negligence with regards to accurate treatment of model parameters is a source of epistemic uncertainty. Contrary to aleatory uncertainty, epistemic uncertainty is sometimes referred to as reducible uncertainty. An increase

in knowledge regarding the physics of a problem, along with accurate modeling, can reduce the amount of this type of uncertainty. Epistemic uncertainty is typically modeled using intervals because the use of probabilistic distributions (even a uniform distribution) can lead to inaccurate predictions in the amount of uncertainty in a system. Upper and lower bounds of these intervals can be drawn from limited experimental data or from expert predictions and judgment.^{8,9}

An additional, special case of epistemic uncertainty is numerical error. This uncertainty is common in numerical modeling and is defined as a recognizable deficiency in any phase or activity of modeling and simulations that is not due to lack of knowledge of the physical system. In CFD, an example of this type of uncertainty would be the discretization error in both the temporal and spatial domains that comes from the numerical solution of the partial differential equations that govern the system.⁹ This uncertainty can be well understood and controlled through code verification and grid convergence studies.

III. Uncertainty Quantification Methodology

This section provides the details of the polynomial chaos techniques used in this study. The first part outlines the general non-intrusive polynomial chaos formulation with the point-collocation approach. The second part details the solution recovery approach for determining the polynomial chaos expansion (PCE) coefficients under sparse conditions. Lastly, a discussion of the error and convergence measures is provided.

A. Point-Collocation Nonintrusive Polynomial Chaos

In recent studies,^{8–12} the polynomial chaos method has been used as a means of UQ over traditional methods, such as Monte Carlo, for computational efficiency. Polynomial chaos is a surrogate modeling technique based on the spectral representation of the uncertainty. An important aspect of spectral representation of uncertainty is that a response value or random function α^* can be decomposed into separable deterministic and stochastic components, as shown in Eq. (1).

$$\alpha^*(\mathbf{x}, \boldsymbol{\xi}) \approx \sum_{i=0}^P \alpha_i(\mathbf{x}) \Psi_i(\boldsymbol{\xi}) \quad (1)$$

Here, α_i is the deterministic component and Ψ_i is the random variable basis functions corresponding to the i^{th} mode. α^* is a function of the vector \mathbf{x} of independent, deterministic variables and the n -dimensional standard random variable vector $\boldsymbol{\xi}$. Note that this series is, by definition, an infinite series. However, in practice, it is truncated and a discrete sum is taken over a number of output modes.¹³ To form a complete basis or for a total order expansion, N_t terms are required, which can be computed from Eq. (2) for a PCE of order p and a number of random dimensions or variables, n .

$$N_t = P + 1 = \frac{(n + p)!}{n!p!} \quad (2)$$

Further details on polynomial chaos theory are given by Ghanem¹⁴ and Eldred.¹³

The objective with any PCE method is to determine the expansion coefficients, α_i . To do this, polynomial chaos methods can be implemented using an intrusive or a non-intrusive approach. While an intrusive method may appear straightforward in theory, for complex problems this process may be time consuming, expensive, and difficult to implement.⁸ In contrast, the non-intrusive approach can be easily implemented to construct a surrogate model that represents a complex computational simulation, because no modification to the deterministic model is required. The non-intrusive methods require only the response (or sensitivity)^{15–17} values at selected sample points to approximate the stochastic response surface.

Several methods have been developed for NIPC. Of these, the point-collocation NIPC method has been used extensively in many aerospace simulations and CFD problems.^{9,10,12,15} The point-collocation method starts with replacing a stochastic response or random function with its PCE using Eq. (1). Then, N_t vectors are chosen in random space and the deterministic code is then evaluated at these points, which is the left hand side of Eq. (1). Following this, a linear system of N_t equations can be formulated and solved for the spectral modes of the random variables. This system is shown in Eq. (3).

$$\begin{pmatrix} \alpha^*(\mathbf{x}, \xi_0) \\ \alpha^*(\mathbf{x}, \xi_1) \\ \vdots \\ \alpha^*(\mathbf{x}, \xi_P) \end{pmatrix} = \begin{pmatrix} \Psi_0(\xi_0) & \Psi_1(\xi_0) & \cdots & \Psi_P(\xi_0) \\ \Psi_0(\xi_1) & \Psi_1(\xi_1) & \cdots & \Psi_P(\xi_1) \\ \vdots & \vdots & \ddots & \vdots \\ \Psi_0(\xi_P) & \Psi_1(\xi_P) & \cdots & \Psi_P(\xi_P) \end{pmatrix} \begin{pmatrix} \alpha_0 \\ \alpha_1 \\ \vdots \\ \alpha_P \end{pmatrix} \quad (3)$$

Note that for this linear system, N_t is the minimum number of deterministic samples required to obtain an analytical solution (i.e., the coefficient vector). If more samples are available and that are linearly independent, the system is considered overdetermined and can be solved using a least squares approach. The number of samples over the required minimum is represented by the use of an oversampling ratio (OSR), defined as the ratio of number of actual samples to the minimum number required (i.e., N_t). In general, the number of collocation points can be determined by multiplying Eq. (2) by an OSR. Hosder et al.¹⁸ determined an effective OSR of two for the stochastic model problems studied. It was shown that the accuracy of the PCE is dependent on the number of collocation points.

Polynomial chaos techniques suffer from a “curse of dimensionality”. This means that the number of deterministic model evaluations required to create an accurate surrogate model grows exponentially with the number of random dimensions. For many large-scale, complex problems, such as those found in modeling hypersonic reentry flows with radiative heat transfer, it may be infeasible or even impossible to obtain even the minimum required number of deterministic model samples. The most desirable approach is to obtain an accurate surrogate model with as few deterministic samples as possible to limit the computational cost, even if the minimum number of samples required for a total order expansion is not achievable.

B. Underdetermined/Sparse Point-Collocation Solution Approach

In general, a system of linear equations that has fewer linearly independent equations than unknowns, possesses an infinite number of solutions. In many PCEs, only a small fraction of the coefficients may carry significant weight in the surrogate model and/or are near zero. This would then allow for an assumption that many of the expansion coefficients are zero, making the vector of expansion coefficients sparse. With this assumption, the linear system can be regularized allowing for a well-posed solution. The objective is to seek out a solution to the linear system with the fewest number of non-zero coefficients. Using convex relaxation, a solution can be obtained from the L_1 -minimization problem shown in Eq. (4).

$$\min \|\alpha\|_1 \text{ subject to } \|\Psi\alpha - \alpha^*\|_2 \leq \delta \quad (4)$$

Here, δ is the truncation error associated with the truncation of the series in Eq. (1). For the problems in this study, δ is assumed equal to zero, as it can be shown that the solution to Eq. (4) is unique in this instance. In the above formulation, the dimensions of Ψ are $N_s \times N_t$ and the vector α^* is of length N_s where $N_s < N_t$ for the underdetermined problem. The vector α is of length N_t . Doostan and Owhadi¹⁹ discuss, in great detail, the theory and formulation of the above method, as well as discussion on stability.

The optimization problem in Eq. (4) is commonly referred to as Basis Pursuit Denoising (BPDN).^{19–21} This type of problem can be solved using many methods from quadratic programming, and the discussion of these methods is left to other works.^{20,21} In the current study, the least absolute shrinkage and selection operator (LASSO) homotopy optimization routine²¹ was selected to find the optimal solution of Eq. (4). While many methods exist for solving the above minimization problem, the homotopy method was selected for efficiency, as this method is not significantly affected by the dimensionality of the problem.²⁰

C. Sample Size, Accuracy, and Convergence

The optimization and sparse solution recovery approach poses two fundamental issues: (1) how to determine the necessary number of samples, N_s , required to obtain an accurate solution and (2) how to measure the accuracy of the solution. The latter of these assumes, of course, that no other means of obtaining the exact solution is possible, thereby relying on the solution obtained from Eq. (4). To reduce the computational cost, the desired approach is to limit the total number of deterministic model evaluations. To address both the sample size and the accuracy issues simultaneously, there must be a measure of the convergence of the expansion coefficients with increasing sample size. The objective of this section is to outline a procedure

for determining an acceptable sample size along with measuring the convergence of the stochastic expansion coefficients.

The first step in this process will be to generate an initial sample set of the random variables. In the current study, the approach will be to use an incremental Latin Hypercube sampling (LHS) to gradually grow the sample set, while maintaining a sample structure that covers the space spanned by the uncertain parameters. Note that this approach is different from that used in previous work by West et al.⁶ where the approach was to take subsets of a larger sample set of size N_t .

The idea is to start with a small LHS structure and evaluate the deterministic model at these points. Then, a first set of PCE coefficients can be obtained using the minimization routine in Eq. (4). This process is then repeated by incrementally expanding the LHS structure, which adds more samples to the minimization problem until the convergence of the expansion coefficients is achieved. Note the incremental LHS only allows for doubling of the sample structure size. This suggests that the sample size may grow rapidly. However, using all of the samples after each LHS increment is not required. A constant sample size increase may still be used by simply taking subsets of each new LHS structure. This may be necessary when tracking convergence.

After the expansion coefficients are approximated, their convergence should be checked at each iteration. In theory, this could be done by monitoring each individual coefficient. Unfortunately, for large scale problems, there may be thousands of coefficients. Also, because the expansion coefficient vector is known to be sparse, this may not be an accurate approach as the degree of sparseness of the solution vector may decrease with increasing sample size causing radical changes in any convergence error measurement. A logical choice for a convergence metric would be to use output statistics based on the expansion coefficients. Sobol indices²² can be used to measure the convergence of the solution and are derived via Sobol Decomposition, which is a variance-based global sensitivity analysis method. First, the total variance, D , can be written in terms of the PCE as shown in Eq. (5).

$$D = \sum_{j=1}^P \alpha_j^2(t, \vec{x}) \langle \Psi_j^2(\vec{\xi}) \rangle \quad (5)$$

Then, as shown by Sudret²² and Crestaux et al.,²³ the total variance can be decomposed as:

$$D = \sum_{i=1}^{i=n} D_i + \sum_{1 \leq i < j \leq n}^{i=n-1} D_{i,j} + \sum_{1 \leq i < j < k \leq n}^{i=n-2} D_{i,j,k} + \cdots + D_{1,2,\dots,n} \quad (6)$$

where the partial variances (D_{i_1,\dots,i_s}) are given by:

$$D_{i_1,\dots,i_s} = \sum_{\beta \in \{i_1,\dots,i_s\}} \alpha_\beta^2 \langle \Psi_\beta^2(\vec{\xi}) \rangle, \quad 1 \leq i_1 < \dots < i_s \leq n \quad (7)$$

Then the Sobol indices (S_{i_1,\dots,i_s}) are defined as,

$$S_{i_1,\dots,i_s} = \frac{D_{i_1,\dots,i_s}}{D} \quad (8)$$

which satisfy the following equation:

$$\sum_{i=1}^{i=n} S_i + \sum_{1 \leq i < j \leq n}^{i=n-1} S_{i,j} + \sum_{1 \leq i < j < k \leq n}^{i=n-2} S_{i,j,k} + \cdots + S_{1,2,\dots,n} = 1.0 \quad (9)$$

The Sobol indices provide a sensitivity measure due to individual contribution from each input uncertain variable (S_i), as well as the mixed contributions ($\{S_{i,j}\}, \{S_{i,j,k}\}, \dots$). As shown by Sudret²² and Ghaffari et al.,²⁴ the total (combined) effect (S_{T_i}) of an input parameter i is defined as the summation of the partial Sobol indices that include the particular parameter:

$$S_{T_i} = \sum_{L_i} \frac{D_{i_1,\dots,i_s}}{D}; \quad L_i = \{(i_1, \dots, i_s) : \exists k, 1 \leq k \leq s, i_k = i\} \quad (10)$$

For example, with $n = 3$, the total contribution to the overall variance from the first uncertain variable ($i = 1$) can be written as:

$$S_{T_1} = S_1 + S_{1,2} + S_{1,3} + S_{1,2,3} \quad (11)$$

From these formulations, it can be seen that the Sobol indices can be used to provide a relative ranking of each input uncertainty to the overall variation in the output with the consideration of nonlinear correlation between input variables and output quantities of interest.

The accuracy of the Sobol indices depend highly on the accuracy of the PCE coefficients, making it an ideal measure of their convergence. Also, because the number of total Sobol indices is the same as the number of uncertain parameters, there is less parameters to track, as this number will always be less than the number of PCE coefficients. To monitor the convergence of the total Sobol indices with the addition of more samples at each iteration, an absolute error, $S_{e_{i,j}}$ can be defined for the j^{th} total Sobol index at iteration i using Eq. (12).

$$S_{e_{i,j}} = \left\| S_{T,i,j} - S_{T,i-1,j} \right\| \quad (12)$$

Note that measuring the convergence based on this absolute error puts emphasis on the variables that contribute to the output uncertainty more significantly. The errors of each total Sobol index, at each iteration, can then be averaged giving a single value for monitoring, which is shown in Eq. (13).

$$\mu_{e,i} = \frac{1}{n} \sum_{j=1}^n S_{e_{i,j}} \quad (13)$$

Plotting this average error at each iteration would then illustrate the convergence of the PCE coefficients. The objective will be to seek out nearly asymptotic convergence, as zero error would likely not be achievable simply due to the randomness of the samples added at each iteration and any numerical inaccuracies that may occur during the analysis of complex models.

D. Dimension Reduction

Previous works by West et al.^{6,26} considered all of the uncertain parameters in the surrogate model used in the final uncertainty analysis. However, in the present study, a much larger set of uncertain parameters will be considered. The expectation is that many of these parameters will weakly contribute to the overall output uncertainty; however, these parameters may introduce noise to the response surface, which may degrade the surrogate model accuracy. Therefore, in this study, the approach will be to reduce the number of uncertain variables with a small number of deterministic model evaluations by using the sparse approximation, point-collocation method and perform an accurate uncertainty analysis for the problem with the reduced dimensions by using, again, the point-collocation NIPC method.

Using the Sobol index based convergence technique outlined in the previous subsection, the objective will be to first determine the parameters which do not contribute significantly to the total output variance. West et al.⁶ showed that a relative ranking of the uncertain parameters can be achieved rapidly, with a small sample set for those problem investigated, even if the accuracy of the surrogate model can still be improved by adding additional samples. While the accuracy of the surrogate model may still be in question with a small sample size, the converged ranking of the uncertain parameters will allow for a systematic means of reducing the number of random dimension to a size that may allow for a more accurate surrogate model that is a function of only those uncertain parameters deemed to be of significant importance. Note that there may be multiple levels of dimension reduction in order to ensure accurate relative ranking of the uncertain parameters as the number of parameters is reduced. In this study, only one level of dimension reduction was sufficient, which is shown in Section V.

IV. Baseline Model and Uncertainty Sources

This section gives the baseline computational model for Earth entry flow with radiative heat transfer over the Stardust capsule geometry. The details of the selected flow solver, the radiation code, and the entry vehicle configuration are given. Then, the entry scenario is presented, which includes selection of freestream conditions and chemical rate models. Uncertainty sources in the computational model are discussed and identified, which will be used in the subsequent uncertainty analysis. A total of 388 uncertain parameters

are identified both in the flow field chemistry and the radiation modeling. Note that all of the uncertainties identified are modeled as epistemic uncertainty due to the lack of knowledge about these parameters.

A. Flow Solver and Geometry

In this study, the flow field was modeled using the LAURA finite-volume, Navier-Stokes flow solver.² This solver uses a second-order, upwind, discretization scheme with tunable relaxation of both inviscid and viscous terms for solution stability. LAURA has been used for many high energy flow studies and has been extensively validated for various atmospheric entry flow scenarios. The flow field was assumed to be steady state with a two-temperature, thermochemical nonequilibrium model.^{27,28}

The Stardust capsule geometry is described by Liu et al.²⁹ The capsule is made up of a 60° sphere cone forebody and a 30° truncated cone backshell. Along the centerline, the capsule is about 55 cm long and the shoulder is about 20 cm behind the nose, along the line of symmetry. Figure 1 shows the axisymmetric grid used in the present study. The grid is made up of 14 blocks, as shown in the upper left image in Figure 1, and is 193 x 267. Note that the block divisions are made by approximate lines of sight from the capsule.

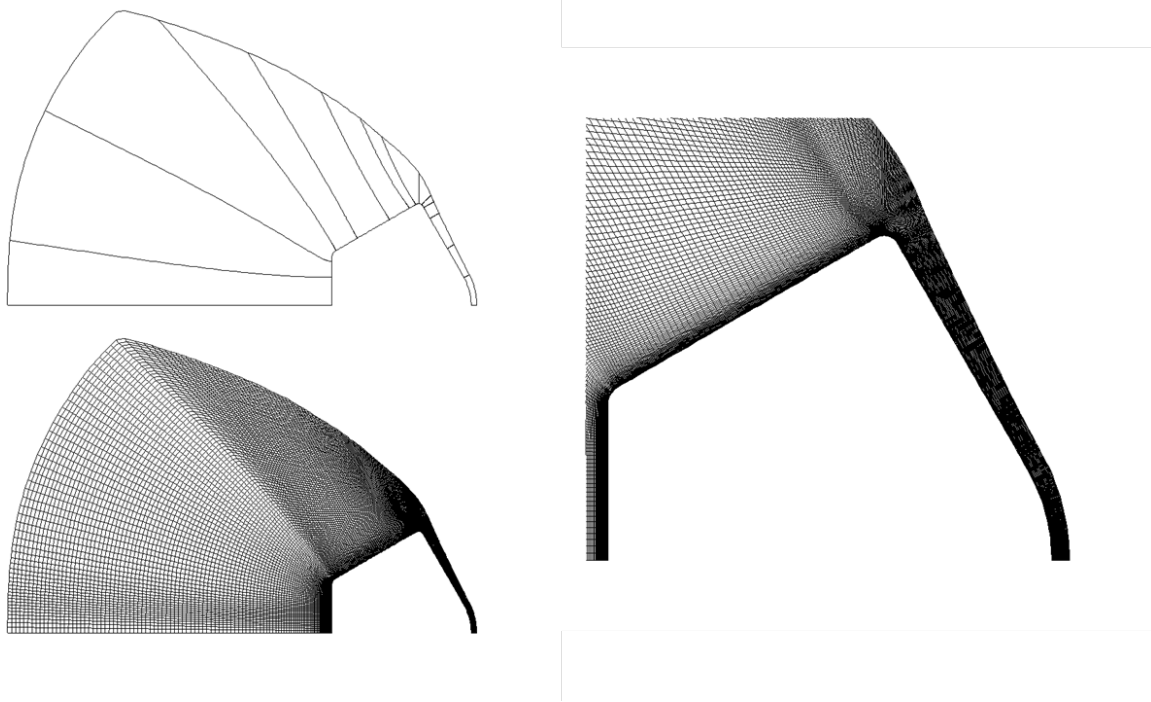


Figure 1: Computational grid.

B. Flow Field Chemistry and Radiation Modeling

In this study, the uncertainty analysis was performed at single point along the trajectory. The 46 second location was selected as this point exhibited the peak radiative heating.¹ At this time, the freestream velocity, density, and temperature were approximately 11.69 km/s, 1.0e-4 kg/m³, and 228 K, respectively. Earth's atmospheric composition was modeled as 76% N₂ and 24% O₂ by mass.

The flow field was modeled with a 26 species composition model: N, N⁺, NO, NO⁺, N₂, N₂⁺, O, O⁺, O₂, O₂⁺, e⁻, C, C⁺, CO, CO₂, C₂, C₃, C₅, C₂H, C₂H₂, CN, H, H⁺, H₂, HCN, CH. A 64 reaction finite rate chemistry model is composed of both reactions due to free-stream composition, as well as reactions that occur due to the introduction of ablation products into the flow field as a result of forebody ablation. The dissociation, exchange, and ionization reactions are listed in Tables A1, A2, and A3, respectively, in the appendix. Notice that in these tables, uncertainty ranges have been included for each of the reactions. The reaction rates and uncertainty ranges are taken from multiple sources.^{30,31}

Forebody ablation was included in the analysis as ablation products can have a significant impact on the afterbody radiative heating.¹ In this study, the ablation is computed assuming a steady-state, equilibrium

phenolic impregnated carbon ablator (PICA) ablation on the forebody, while the non-ablating afterbody is assumed in radiative equilibrium with a fully-catalytic to homogeneous recombination wall boundary condition. Note that the wall catalyst model on a non-ablating surface has a negligible effect on the surface radiative heating.³¹

Figure 2(a) shows the mass fraction of CO in the afterbody due to forebody ablation. Note that CO is the dominant ablation product and also a known strong radiator. The difference in the intensity along the line of sight specified in Figure 2(a) is shown in Figure 2(b). Notice that ablation causes a nearly 40% rise in the intensity near the wall. Johnston and Brandis¹ point out that this increase in the intensity is not a result of radiation from the ablation products, but rather the effect of the ablation products on the vibrational-electronic energy by lowering the vibrational-electronic temperature in the boundary layer. The ablation products reduce absorption in the afterbody flow field boundary layer, thereby increasing the radiative heat flux at the wall.

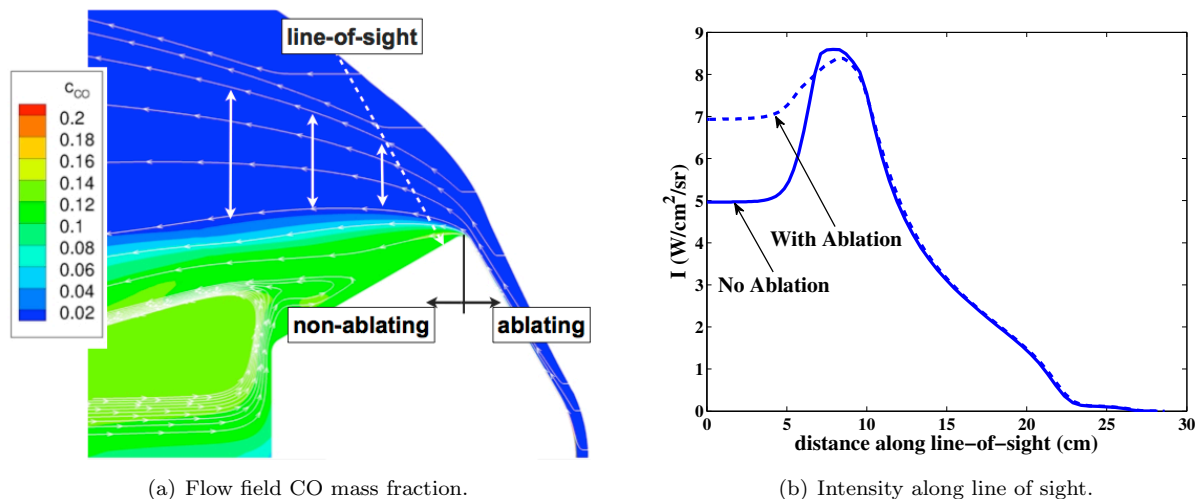


Figure 2: Contour of CO mass fraction and ablation product effect on intensity.

The radiation was modeled using the High-Temperature Aerothermodynamic Radiation (HARA) code.^{3,4} The HARA model is based on a set of atomic levels and lines obtained from the National Institute of Standards and Technology (NIST) database,³² Opacity Project databases,³³ and atomic bound-free (photoionization) cross-sections from the TOPbase.³⁴ In the present study, the flow field solver and the radiative heat transfer calculations are coupled. HARA uses a Collisional Radiative (CR) or non-Boltzmann modeling of atomic and molecular electronic states. This is based on a set of electronic and heavy particle impact excitation rates. The non-Boltzmann approach used in this study is described by Johnston et al.³¹

Previous studies have shown that emission and absorption from atomic nitrogen and oxygen lines plays a key part in the radiation.⁵ Johnston and Brandis¹ showed that afterbody radiation is due large in part to atomic lines in vacuum ultra-violet (VUV) portion of the spectrum. The presence of these lines are the result of electronic transitions between an upper level $j \geq 4$ and a lower levels $i \leq 3$. In the present study, the lines considered as uncertain are listed in Tables A5 and A6 for N and O, respectively. Note that there are some lines being considered that have an upper level $j \geq 1$ and a lower level $i \leq 10$, as these lines may also contribute to the radiation. These tables also list the oscillator strength and Stark broadening width uncertainty ranges adopted by Johnston and Kleb.⁵ In addition to the atomic lines, photoionization cross-sections for N and O are also treated as uncertain. A total of 35 N and 32 O photoionization cross-sections, all with $\pm 20\%$ uncertainty are considered in the present study. Note that the uncertainty in these parameters were also obtained from Johnston and Kleb.⁵

Electron impact excitation rates for atomic N and O have been shown to be the most significant processes in the non-Boltzmann calculation.⁵ The baseline rates for these processes are provided by Johnston et al.⁴ It was found in this work that electron impact excitation processes with upper levels $j \geq 1$ and lower levels $i \leq 10$ are the most important for backshell radiative heating predictions, which allowed the present work to include only these 45 transitions in the uncertainty analysis. A comparison of multiple sources for these rates is made by Johnston and Kleb,⁵ who show that an order of magnitude uncertainty covers the range of

rates proposed by various researchers. This \pm one order of magnitude uncertainty is applied in this work for electron-impact excitation rates of N and O.

Molecular band systems of both air species and ablation products are treated using the smeared-rotational band approach (SRB). This approximation is shown by Johnston et al.³ to result in errors of less than 3% for air shock layers with ablation products. Oscillator strength and non-Boltzmann excitation rate uncertainties proposed by Johnston and Kleb⁵ for air species and Johnston et al.³¹ for ablation products are applied in this work. For example, Tables A7 and A8 present the non-Boltzmann excitation rate uncertainties for CN and CO obtained from these studies and applied in this work. Even with the up to ± 2 order of magnitude uncertainties shown in Tables A7 and A8, these uncertainties will be shown to have a negligible impact on the backshell radiation uncertainty. This is a result of the weak contribution from molecular band systems to the backshell radiation.

Johnston and Kleb⁵ discuss that there is significant uncertainty in negative ion continuum cross section. Johnston et al.³ provide the baseline values used in the is study and an uncertainty of $\pm 100\%$ was used to capture differences in theoretical predictions and experimental measurements.⁵

A sensitivity analysis of two-temperature modeling parameters identified the electronic-translational energy relaxation (defined in Eq. 65 of Gnoffo et al.²⁷) as the most important for backshell radiation. This parameter essentially governs the equilibration of the two-temperatures in the backshell region. To capture potential uncertainties in the energy exchange cross section applied for neutral-electron collisions, a \pm one order of magnitude uncertainty is applied to this cross section for N and O.

The nonequilibrium radiation code uses a tangent-slab approximation for computing the radiative flux and its divergence; however, Johnston and Brandis¹ showed that the tangent-slab approximation can cause the afterbody radiation to be over predicted in the afterbody region. Figure 3 shows the difference in radiative heating profile along the centerline of the geometry for the tangent-slab approach versus a full ray-tracing approach.³⁵ This approach rotates the axisymmetric solution to form a three dimensional solution. Then, the radiative intensity is computed along numerous rays at each body point. In the forebody, the tangent-slab approach only slightly over predicts the radiative heating. However, approaching the shoulder and into the afterbody, the over prediction can be nearly 35%. While the tangent-slab approach is less computationally demanding, the approach in this study will be to use the full ray-tracing procedure to improve the accuracy of the analysis. Note that the radiation values in this work are slightly different than shown in the work by Johnston and Brandis¹ due to a slight change in a numerical algorithm. A new approach for scaling the quasi steady-state (QSS) matrix was implemented to allow for more robust matrix inversions at vibrational-electronic temperatures below roughly 4500 K.

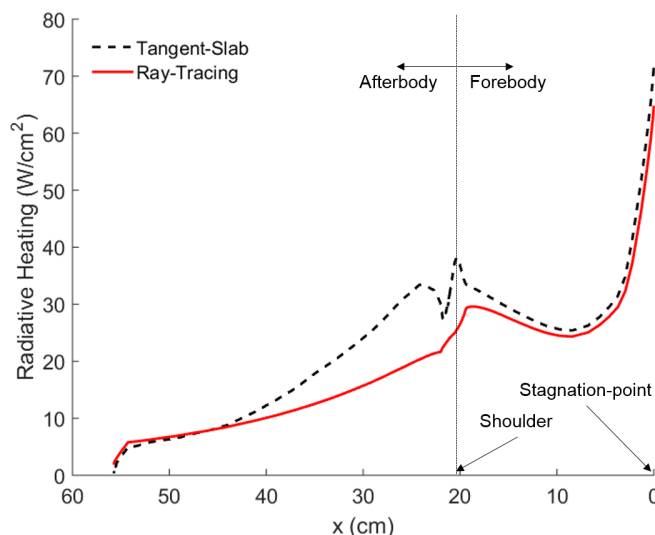


Figure 3: Comparison of ray-tracing and tangent-slab backshell radiative heat flux calculations.

C. Baseline Results

Prior to constructing the surrogate model and performing the uncertainty analysis, a baseline solution was obtained with the nominal values of the uncertain modeling parameters considered in this study. Flow field contours of pressure and vibrational-electronic temperature are shown in Figure 4. The pressure contour in Figure 4(a) shows a well-defined shock layer in the forebody, that dissipates around the shoulder of the capsule.

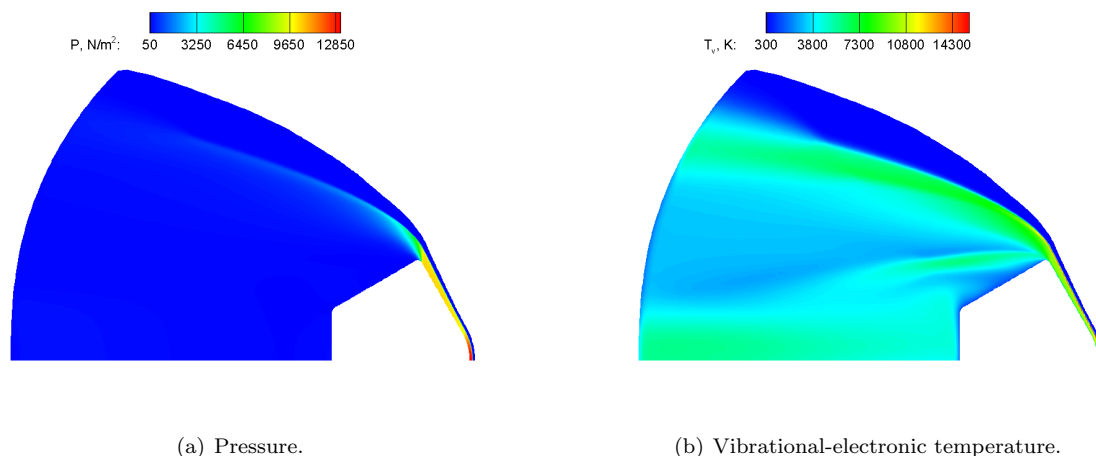


Figure 4: Baseline Solution contours of pressure and vibrational temperature.

The contour of the vibrational-electronic temperature shown in Figure 4(b) provides some key insight into the source of the afterbody radiation. Notice in the afterbody region the three temperature regions. Johnston and Brandis¹ discuss that a large contribution to the backshell emission comes from the cooler vibrational-electronic temperature region (less than 5000 K), which indicates a region of significant chemical non-equilibrium. This lower temperature region possesses a high number densities of N and N⁺, which is an indication of a strong radiative region of non-equilibrium expanding flow. Moving closer to the wall, there is an increase in the vibrational-electronic temperature that creates a region of strong absorption.

The magnitude of the radiation in the afterbody is shown in Figure 5, in comparison to the laminar convective heating. Notice that the radiative heating is significantly larger than the convective heating. This emphasizes the importance of accurate modeling of the radiation in the afterbody region as this heating is clearly not negligible.

With a converged, baseline solution, the approach will be to perturb it for performing the uncertainty and sensitivity analyses. This will reduce the computational time required for a converged solution when only small changes to input parameters are made.

V. Results and Discussion

A. Sensitivity Analysis

Recall from section IV that there are a total of 388 uncertain parameters considered in this study. As a result, propagating the uncertainty with a second order PCE would require a minimum of 75855 evaluations of the CFD model to construct a total order expansion (from Eq. (2)). While this number of runs may still be less than required for a converged Monte Carlo solution, this number of runs is not feasible in this study due to the computational cost of the model. The objective will be to reduce this number to a more manageable and reasonable size by constructing the surrogate model with only those parameters that significantly contribute to the uncertainty in the radiative heating on the backshell.

Following the approach outlined in section III, an initial Latin hypercube structure of 50 samples was generated using all 388 uncertain variables. A sparse approximation of the PCE was then constructed

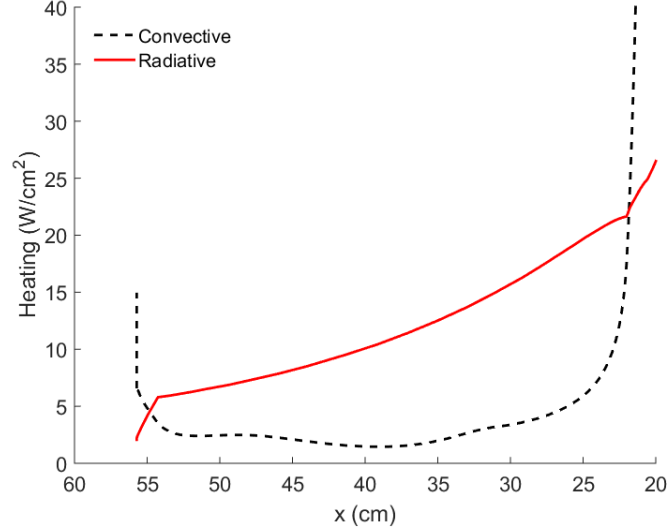


Figure 5: Convective and radiative afterbody heating.

(Eq. (4)) and the total Sobol indices calculated (Eq. (9)) iteratively for an increasing sample size from 2 to 50 by 2 samples. This approach allows for tracking of the convergence of the Sobol indices (Eqs. (12) and (13)). Based on these results the sample set of 50 was doubled to 100 using incremental Latin hypercube to preserve the sample structure and coverage within the domain of the uncertain parameters. Construction of the sparse PCE and Sobol indices calculation was then continued from 50 to 100 samples.

The convergence of the Sobol indices is illustrated in Figure 6 in two ways. First, Figure 6(a) shows a plot of the convergence of the maximum relative change among all of the uncertain parameters at a body point about 23 cm from the nose, which translates to a point just behind the shoulder. At 50 samples, there was a change of about 11%, but increasing the sample size to 100 reduced the maximum change to only 2%. Figure 6(b) shows the convergence of all of the total Sobol indices. While there are 388 curves on this figure, clearly there are only about four parameters that are found to be of importance as the number of samples approaches 100. These four will be identified and discussed later. Note that the non-smooth convergence results are expected as there is no guarantee of monotonicity with a point-collocation approach with an unstructured sampling approach.

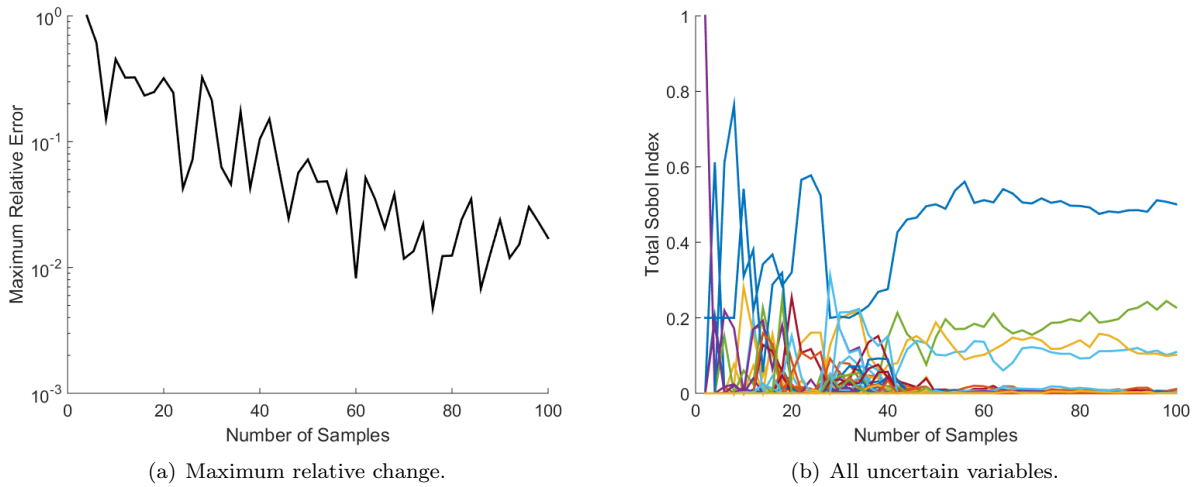


Figure 6: Convergence of total Sobol indices.

Given the convergence of the relative ranking of the Sobol indices, no additional samples were added to the structure. Note that the surrogate (i.e., the PCE coefficients) may not be accurate at a desired level,

but the variance is converged enough such that ranking information can be extracted with a high degree of confidence.

Figure 6 shows the Sobol convergence at one point on the backshell. Using all 100 samples, the Sobol indices were calculated along the remainder of the backshell and plotted in Figure 7. All 388 parameters are plotted in Figure 7(a). The most interesting note here is that regardless of position on the backshell, the output variance is driven by the same four parameters even though their relative ranking changes with position. These top four are plotted in Figure 7(b). Notice that these four parameters contribute to more than 90% of the output variance of the radiative heat flux and this is constant for the majority of the backshell.

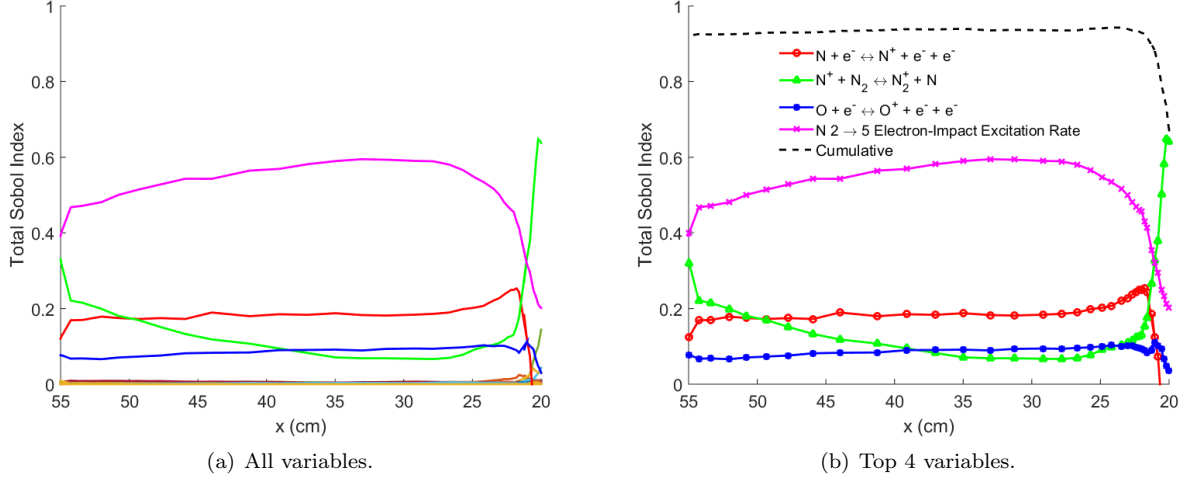


Figure 7: Sobol index values along the backshell.

The sensitivity of the radiation to these top four parameters can further be investigated by considering each individually. Figure 8 shows the individual parameter contributions to the radiative heating uncertainty on the backshell. Note that these results were obtained by applying only the uncertainty to individual rates. No other uncertainties are included. Also, in the afterbody, the radiation magnitude has a monotonic dependency on the uncertainty in these four parameters. Applying the maximum and minimum values of the uncertainty captures the range of radiation variation.

Johnston and Brandis¹ note that the primary contributor to the radiation are the vacuum ultraviolet lines for N and O, which result from electronic transitions between upper and lower levels of these atoms. The sensitivity results align with this fact in the sense that the parameters that most impact the uncertainty in the radiation are those that influence N and O number densities and electronic transition rates.

Three of the four most significant uncertainty sources are flow field reaction rates. Figure 8(a) shows the impact of uncertainty for the $N + e^- \leftrightarrow N^+ + e^- + e^-$ rate and Figure 8(b) shows the impact of the $O + e^- \leftrightarrow O^+ + e^- + e^-$ rate. There is a significant contribution to the uncertainty from $N + e^- \leftrightarrow N^+ + e^- + e^-$ rate, even through the uncertainty is only $\pm 50\%$ of the nominal rate. Also, notice that in Figure 8(a) and 8(b) the sensitivity of the radiation to these parameters is only significant on the backshell. Because the radiation on the forebody is dominated by equilibrium radiation, it is insensitive to the $\pm 50\%$ uncertainty in ionization rates. While N and O are ionized in the forebody to form N^+ and O^+ , the rate of deionization in the afterbody affects the number densities of N and O in the afterbody region. Note that in the recombining, expanding flow of the afterbody, the reverse process for the ionization reactions (recombination) are dominant. Because the backward rate is computed as the ratio of the forward rate and equilibrium constant, the uncertainties applied to the forward rates are also applied to the backward rates. This is why reducing the forward rates increases the radiative heating.

The order-of-magnitude reductions in the $N^+ + N_2 \leftrightarrow N_2^+ + N$ rate is seen to increase the radiation in both the forebody and backshell regions. In the forebody region, this decreased rate leads to more N^+ in the nonequilibrium post shock region, which leads to increased emission. In the backshell region, this rate has a similar impact, although it occurs in the shear layer.

The last of the four important uncertain variables is the electronic-impact excitation rate for N between level 2 and level 5. This single rate is interesting. 45 total excitation rates were considered uncertain in this

study, yet only this one reaction was found to be sensitive to the uncertainty. In comparison, the level 3 to 5 rate is larger than the 2 to 5 rate. However, similar to the flow field reactions, the reverse processes are what is important. The deexcitation rate from level 5 to 2 is three times the rate from level 5 to 3. This is true for all of the rates between upper levels greater or equal to 4 and lower levels less than or equal to 3. Note also that the uncertainty in this rate does not impact the forebody radiation and is unique to the backshell heating.

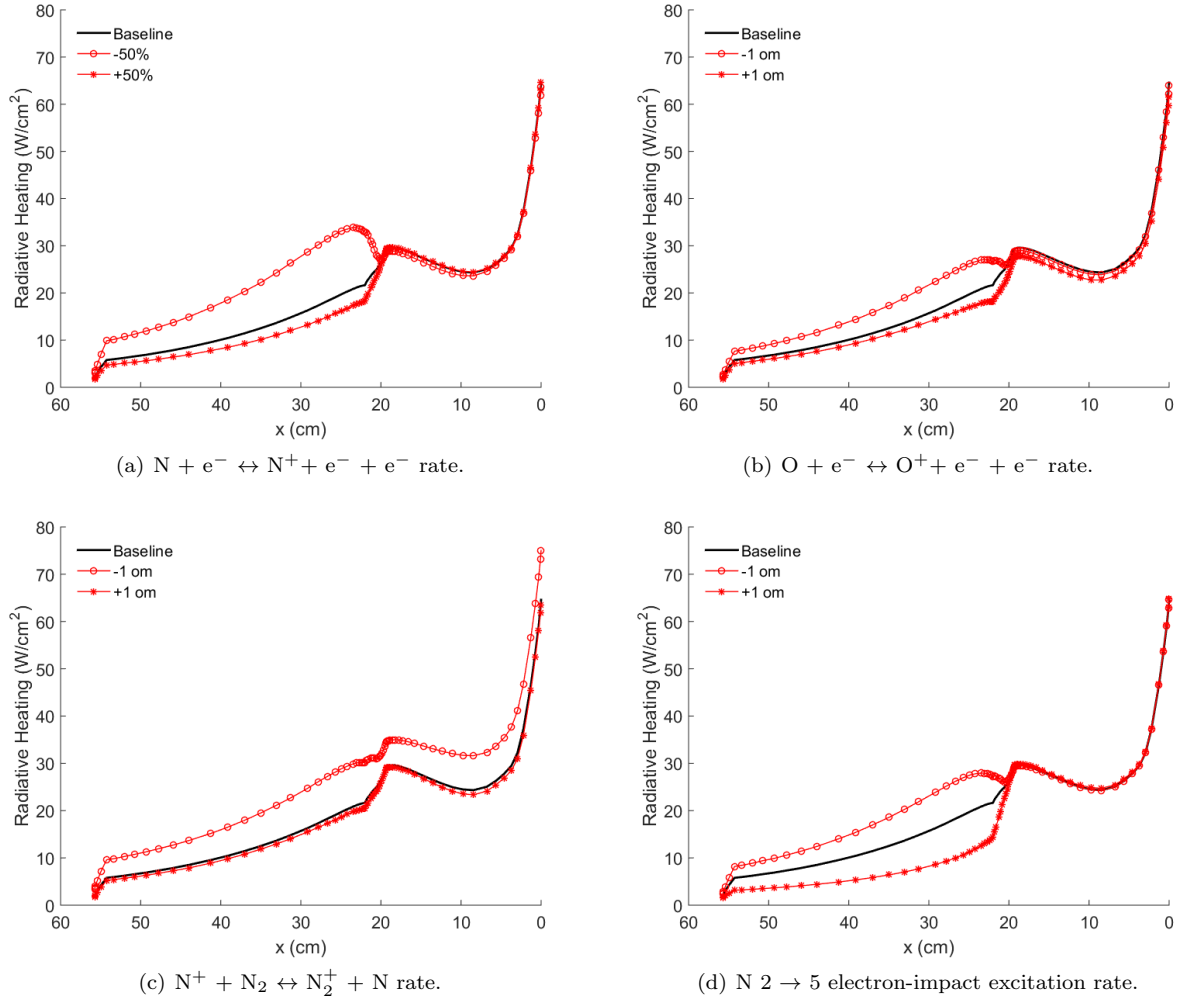


Figure 8: Individual parameter uncertainty contributions to radiative heating.

B. Dimension Reduction and Uncertainty Propagation

With the 388 uncertain variables reduced to only 4, an estimate of the uncertainty can quickly and accurately be calculated. A second order PCE surrogate model was constructed using 30 evaluations of the CFD model, which is twice the minimum required for a total order expansion ($OSR = 2$). The uncertainty was then propagated through the surrogate model via Monte Carlo sampling with 10^7 samples. The uncertainty band, along with the total Sobol index values for each parameter along the surface of the backshell are shown in Figure 9. Note that the uncertainty band in Figure 9(a) has no probabilistic interpretation because the uncertain inputs were all considered to be epistemic and are not probabilistic in nature. This band is merely the worst-case or extrema of the output uncertainty as a function of spatial location along the backshell of the vehicle. The uncertainty band is, at a maximum, 125% above and about -50% below the nominal prediction. The location of greatest uncertainty is just behind the shoulder, around 25 cm from the stagnation point. Clearly, the uncertainty in just the four key parameters produces a significant amount of uncertainty in the radiation prediction.

The Sobol indices in Figure 9(b) are shown to confirm the trend observed in the sensitivity analysis/dimension reduction study discussed in the previous section. Compared to Figure 7(b), a similar trend is observed; however, the actual Sobol values are slightly different. This is expected given the improved accuracy of the reduced dimension surrogate model compared to the sparse approximation with all 388 variables in addition to the small amount of uncertainty neglected as a result of the dimension reduction. As stated previously this information can be used to effectively allocate resources to improve radiation modeling and reduce uncertainty in modeling parameters. Also, Figure 9 only shows the backshell region because the forebody will have different sensitivities than the afterbody. This was previously investigated by Johnston and Kleb.⁵

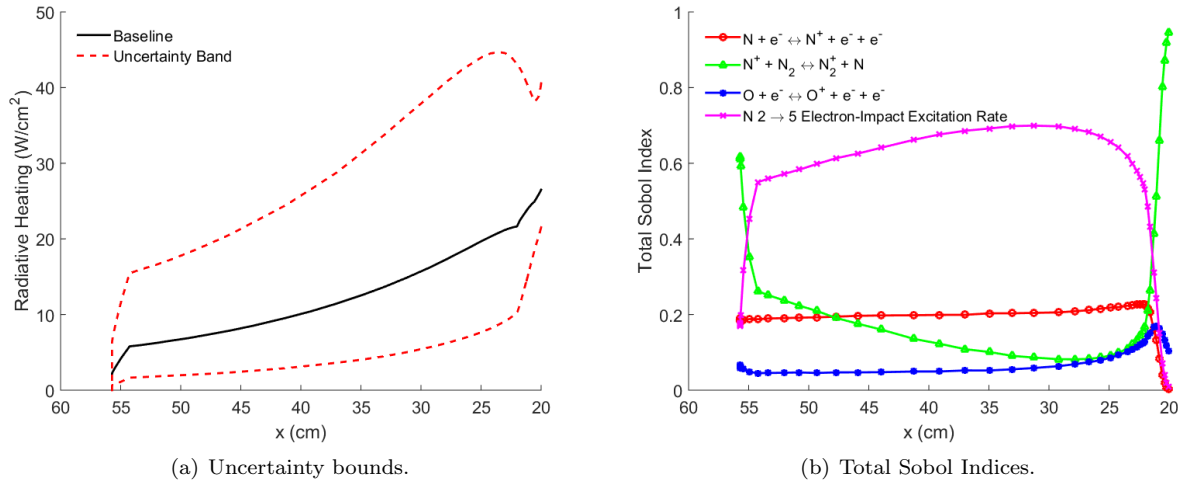


Figure 9: Sensitivities and uncertainty band of backshell radiation (reduced dimension analysis).

To validate the accuracy of the final surrogate model, a series of test points were used throughout the design space for comparison to the surrogate. Consistently, the surrogate model, on average, was within 2 to 3 % of the test points for the entirety of the backshell region, even at the corners of the domain where large errors are often observed. This result suggests that a 2nd order fit was adequate for this analysis and results for the uncertainty propagation were accurate.

VI. Conclusions

During high-speed Earth entry, radiation can significantly increase the surface heating of an entry vehicle including the afterbody region. Accurate uncertainty analysis of shock-layer radiation during earth entry poses significant challenges due to the complexity of the numerical models and the sheer number of modeling parameters that are not well understood or not well characterized. In this study, an efficient and accurate approach for sensitivity analysis and uncertainty quantification of afterbody radiative heating was introduced, which was based on dimension reduction in uncertainty space and performing accurate uncertainty analysis in the reduced dimension. The approach was applied to the analysis of afterbody radiation on the backshell of the Stardust capsule at the peak afterbody radiation trajectory point. This model contained nearly 400 uncertain parameters, which was reduced to only four by using a combined sparse approximation and variance-based sensitivity calculation with the point-collocation non-intrusive polynomial chaos approach. Greater than 90% of the uncertainty was captured with only 130 high-fidelity CFD solutions. This relatively small number of samples used to estimate the uncertainty and perform a sensitivity analysis is significant compared to sampling-based approaches.

The global, nonlinear, sensitivity approach used in this study was critical in this particular analysis for dimension reduction and ranking of the significant uncertain variables, as a local sensitivity analysis (e.g., finite differencing) could be misleading given the large input uncertainty ranges and possible nonlinear dependence of the radiation on the significant parameters. The initial sensitivity analysis showed that only four parameters contributed significantly to the backshell radiation uncertainty: the electronic-impact

excitation rate for N between level 2 and level 5 and rates of three chemical reactions influencing N, N⁺, O, and O⁺ number densities in the flow field. A reduced dimension surrogate model was then constructed and used to efficiently propagate the uncertainty, which showed an uncertainty interval as wide as +125% and -50% of the nominal case.

Overall, this approach demonstrated a means of quantifying the uncertainty in large-scale, complex CFD models. In particular, CFD models of planetary entry flows and radiative heating pose significant challenges for uncertainty quantification and sensitivity analysis due to the complex physics being modeled, computational cost of the models, and the number of input uncertain parameters. The results of this analysis will aid in the allocation of resources for model improvement, experimental testing, design changes and overall risk reduction.

References

- ¹Johnston, C. O. and Brandis, A. M., "Feature of Afterbody Radiative Heating for Earth Entry," Vol. 52, 2015, pp. 105–119.
- ²Mazaheri, A., Gnoffo, P. A., Johnston, C. O., and Kleb, B., "LAURA Users Manual: 5.4-54166," Tech. rep., NASA/TM-2011-217092, May 2009.
- ³Johnson, C. O., Hollis, B. R., and Sutton, K., "Spectrum Modeling for Air Shock-layer Radiation at Lunar-Return Conditions," *Journal of Spacecraft and Rockets*, Vol. 45, No. 5, 2008, pp. 865–878.
- ⁴Johnson, C. O., Hollis, B. R., and Sutton, K., "Non-Boltzman Modeling for Air Shock Layers at Lunar Return Conditions," *Journal of Spacecraft and Rockets*, Vol. 45, No. 5, 2008, pp. 879–890.
- ⁵Johnston, C. O. and Kleb, B., "Uncertainty Analysis of Air Radiation for Lunar-Return Shock Layers," *Journal of Spacecraft and Rockets*, Vol. 49, No. 3, 2012, pp. 425–434.
- ⁶West IV, T. K. and Hosder, S., "Uncertainty Quantification of Hypersonic Reentry Flows with Sparse Sampling and Stochastic Expansions," *Journal of Spacecraft and Rockets*, Vol. 52, No. 1, 2015, pp. 120–133.
- ⁷Oberkampf, W. L., Helton, J. C., and Sentz, K., "Mathematical Representation of Uncertainty, AIAA 2001-1645," 3rd Non-Deterministic Approaches Forum, Seattle, WA, April 2001.
- ⁸Hosder, S. and Bettis, B., "Uncertainty and Sensitivity Analysis for Reentry Flows with Inherent and Model-Form Uncertainties," *Journal of Spacecraft and Rockets*, Vol. 49, No. 2, 2012, pp. 193–206.
- ⁹Bettis, B., Hosder, S., and Winter, T., "Efficient Uncertainty Quantification in Multidisciplinary Analysis of a Reusable Launch Vehicle, AIAA 2011-2393," 17th AIAA International Space Planes and Hypersonic Systems and Technologies Conference, San Francisco, CA, April 2011.
- ¹⁰Hosder, S., Walters, R. W., and Balch, M., "Point-Collocation Nonintrusive Polynomial Chaos Method for Stochastic Computational Fluid Dynamics," *AIAA Journal*, Vol. 48, No. 12, 2010, pp. 2721–2730.
- ¹¹Witteveen, J. A. S. and Bijl, H., "Efficient Quantification of the Effect of Uncertainties in AdvectionDiffusion Problems Using Polynomial Chaos," *Numerical Heat Transfer*, Vol. 53, No. 5, 2008, pp. 437–465.
- ¹²Han, D. and Hosder, S., "Inherent and Model-Form Uncertainty Analysis for CFD Simulation of Synthetic Jet Actuators, AIAA 2012-0082," 48th AIAA Aerospace Sciences Meeting, Nashville, TN, Jan. 2012.
- ¹³Eldred, M. S., "Recent Advances in Non-Intrusive Polynomial Chaos and Stochastic Collocation Methods for Uncertainty Analysis and Design, AIAA 2009-2274," 50th AIAA/ASME/ASCE/AHS/ASC Structures, Palm Springs, CA, May 2009.
- ¹⁴Ghanem, R. G. and Spanos, P. D., *Stochastic Finite Elements: A Spectral Approach*, Springer-Verlag, New York, 1991.
- ¹⁵West IV, T. K., Hosder, S., and Johnston, C. O., "Multi-Step Uncertainty Quantification Approach Applied to Hypersonic Reentry Flows," *Journal of Spacecraft and Rockets*, Vol. 51, No. 1, 2014, pp. 296–310.
- ¹⁶Lockwood, B. and Mavriplis, D., "Gradient-Based Methods for Uncertainty Quantification in Hypersonic Flows," *Computers and Fluids Journal*, Vol. 85, Oct. 2013, pp. 27–38.
- ¹⁷Roderick, O., Anitescu, M., and Fischer, P., "Polynomial Regression Approaches Using Derivative Information for Uncertainty Quantification," *Nuclear Science and Engineering*, Vol. 164, No. 2, 2010, pp. 122–139.
- ¹⁸Hosder, S., Walters, R. W., and Balch, M., "Efficient Sampling for Non-Intrusive Polynomial Chaos Applications with Multiple Uncertain Input Variables, AIAA 2007-1939," 48th AIAA/ASME/ASCE/AHS/ASC Structures, Structural Dynamics, and Materials Conference, Honolulu, HI, April 2007.
- ¹⁹Doostan, A. and Owghadi, H., "A non-adapted sparse approximation of PDEs with stochastic inputs," *Journal of Computational Physics*, Vol. 230, No. 8, 2011, pp. 3015–3034.
- ²⁰Yang, A., Ganesh, A., Sastry, S., and Ma, Y., "Fast L1-Minimization Algorithms and An Application in Robust Face Recognition: A Review," Tech. Rep. UCB/EECS-2010-13, EECS Department, University of California, Berkeley, Feb 2010.
- ²¹Asif, M. S. and Romberg, J., "Fast and Accurate Algorithms for Re-Weighted l_1 -Norm Minimization," *IEEE Transactions on Signal Processing*, Vol. 61, No. 23, 2013, pp. 5905–4916.
- ²²Sudret, B., "Global sensitivity analysis using polynomial chaos expansion," *Reliability Engineering and System Safety*, Vol. 93, No. 7, 2008, pp. 964–979.
- ²³Cresta, T., Maitre, O. L., and Martinez, J.-M., "Polynomial chaos expansion for sensitivity analysis," *Reliability Engineering and System Safety*, 2009.
- ²⁴Ghaffari, S., Magin, T., and Iaccarino, G., "Uncertainty Quantification of Radiative Heat Flux Modeling for Titan Atmospheric Entry, AIAA 2010-239," 48th AIAA Aerospace Sciences Meeting Including the New Horizons Forum and Aerospace Exposition, Orlando, FL, Jan. 2010.

- ²⁵Blatman, G. and Sudret, B., “Adaptive sparse polynomial chaos expansion based on least angle regression,” *Journal of Computational Physics*, Vol. 230, No. 6, 2011, pp. 2345–2367.
- ²⁶West IV, T. K., Brune, A. J., Hosder, S., and Johnstons, C. O., “Uncertainty Analysis of Radiative Heating Predictions for Titan Entry,” *Journal of Thermophysics and Heat Transfer*, 2015.
- ²⁷Gnoffo, P. A., Gupta, R. N., and Shinn, J. L., “Conservation Equations and Physical Models for Hypersonic Air Flows in Thermal and Chemical Nonequilibrium,” Tech. rep., NASA TP 2867, Feb. 1989.
- ²⁸Park, C., Howe, J. T., Jaffe, R. L., and Candle, G. V., “Review of Chemical-Kinetic Problems for Future NASA Missions, II: Mars Entries,” *Journal of Thermophysics and Heat Transfer*, Vol. 8, No. 1, 1994, pp. 9–23.
- ²⁹Liu, Y., Prabhu, D., Trumble, K. A., Saunders, D., and Jenniskens, P., “Radiation Modeling for the Reentry of the Stardust Sample Return Capsule,” *Journal of Spacecraft and Rockets*, Vol. 47, No. 5, 2010, pp. 741–752.
- ³⁰Gokcen, T., “N₂-CH₄-Ar Chemical Kinetic Model for Simulations of Atmospheric Entry to Titan,” *Journal of Thermophysics and Heat Transfer*, Vol. 21, No. 1, 2007, pp. 9–18.
- ³¹Johnston, C. O., Brandis, A. M., , and Sutton, K., “Shock Layer Radiation Modeling and Uncertainty for Mars Entry, AIAA 2012-2866,” 43rd AIAA Thermophysics Conference, New Orleans, LA, June 2012.
- ³²Ralchenko, Y., “NIST Atomic Spectra Database, Version 3.1.0,” .
- ³³The Opacity Project Team, *The Opacity Project*, Vol. 1, 1995.
- ³⁴Cunto, W., Mendoza, C., Ochsenbein, F., and Zeppen, C., “TOPbase at the CDS,” *Astronomy and Astrophysics*, Vol. 275, 1993, pp. L5–L8.
- ³⁵Mazaheri, A., Johnston, C. O., and Sefidbakht, S., “Three-Dimensional Radiation Ray-Tracing for Shock-Layer Radiative Heating Simulations,” *Journal of Spacecraft and Rockets*, Vol. 50, No. 3, 2013, pp. 485–493.

Appendix

The following appendix gives tables of the four groups of uncertain parameters for the radiative heat transfer model problem used in this study. Note that the parameters of Tables A1, A2, A3, A7, and A8 are those of an Arrhenius form. The equations for each of these three tables are given by Eq. (14), (15), and (16), respectively. The notation “om” on the uncertainty ranges denotes order-of-magnitude.

Table A1: Flow Field Dissociation Reactions

#	Reaction	$A_{f,i}$	$n_{f,i}$	$D_{f,i}$	$T_{f,i}$	Third Body, M	Uncertainty
Dissociation Reactions							
1	$C_2 + M \leftrightarrow 2C + M$	4.5e+18	-1.00	7.15e+04	T_a	All	+1, -1 om
2	$C_2H + M \leftrightarrow C_2 + H + M$	1.7e+35	-5.16	5.74e+4	T_a	All	+1, -1 om
3	$C_2H_2 + M \leftrightarrow C_2H + H + M$	4.0e+16	0.00	5.40e+4	T_a	All	+1, -1 om
4	$C_3 + M \leftrightarrow C_2 + C + M$	1.68e+21	-1.50	8.774e+04	T_a	H, C, N, O	+1, -1 om
		8.4e+20	-1.50	8.774e+04	T_a	others	+1, -1 om
		4.0e+14	0.00	81549.0	T_{tr}	All	+1, -1 om
5	$C_5 + M \leftrightarrow C_3 + C_2 + M$	4.0e+14	0.00	3.3717e+04	T_a	All	F=2.0
6	$CH + M \leftrightarrow C + H + M$	1.9e+14	0.00	7.100e+04	T_a	All	+1, -1 om
7	$CN + M \leftrightarrow C + N + M$	6.0e+15	-0.40	1.2270e+5	T_a	H, C, N, O	+50, -75%
8	$CO + M \leftrightarrow C + O + M$	1.15e+11	1.519	1.2270e+5	T_a	CO ₂	+50, -75%
		1.15e+10	1.519	1.2270e+5	T_a	others	+50, -75%
		2.3e+10	1.519	1.2270e+5	T_a	others	+50, -75%
9	$CO_2 + M \leftrightarrow CO + O + M$	1.185e+22	-1.50	63275.0	T_a	H, C, N, O	+0, -1 om
		7.9e+21	-1.50	63275.0	T_a	others	+0, -1 om
		0	0.00	4.840e+04	T_a	H	F=2.0
10	$H_2 + M \leftrightarrow 2H + M$	9.0e+14	0.00	4.840e+04	T_a	others	F=2.0
11	$HCN + M \leftrightarrow CN + H + M$	3.57e+26	-2.60	6.2845e+04	T_a	All	F=2.0
12	$N_2 + M \leftrightarrow 2N + M$	3.01e+22	-1.60	1.132e+05	T_a	H, C, O, N	+1, -1 om
		7.000e+21	-1.60	1.132e+05	T_a	others	+1, -1 om
		4.567e+17	0.00	7.550e+04	T_a	H, C, N, O, NO, CO ₂	+1, -1 om
13	$NO + M \leftrightarrow N + O + M$	2.080e+16	0.00	7.550e+04	T_a	others	+1, -1 om
		1.000e+22	-1.50	5.936e+04	T_a	H, C, O, N	+50, -50%
		2.000e+21	-1.50	5.936e+04	T_a	others	+50, -50%

$$k_{f,i} = A_{f,i} T_{f,i}^{n_{f,i}} \exp(-D_{f,i}/T_{f,i}) \quad (14)$$

$$K_{f,ij}^{hp} = A_{hp} \left(\frac{T_a}{6000} \right)^{n_{hp}} \exp(-E_{hp}/T_a) \quad (15)$$

$$K_{f,ij}^{el} = A_{el} T_{ve}^{n_{el}} \exp(-E_{el}/T_{ve}) \quad (16)$$

Table A2: Flow Field Exchange Reactions

#	Reaction	$A_{f,i}$	$n_{f,i}$	$D_{f,i}$	$T_{f,i}$	Uncertainty
15	$C_2 + C_2H_2 \leftrightarrow 2C_2H$	1.1e+14	-0.38	6.87e+3	T_{tr}	+1, -1 om
16	$C_2 + N_2 \leftrightarrow CN + CN$	1.50e+13	0.0	2.1e+4	T_{tr}	+1, -1 om
17	$C_2H + H \leftrightarrow C_2 + H_2$	1.600e+13	0.15	1.460e+04	T_{tr}	+1, -1 om
18	$C_3 + C \leftrightarrow C_2 + C_2$	6.00e+11	1.07	1.650e+04	T_{tr}	+1, -1 om
19	$C_3 + N \leftrightarrow CN + C_2$	1.000e+12	0.00	3.420e+04	T_{tr}	+1, -1 om
20	$CH + C \leftrightarrow C_2 + H$	2.00e+14	0.0	0.0	T_{tr}	+1, -1 om
21	$CH + CO \leftrightarrow C_2H + O$	2.5e+10	0.67	3.90e+4	T_{tr}	+1, -1 om
22	$CH + N_2 \leftrightarrow HCN + N$	4.40e+12	0.0	1.106e+04	T_{tr}	+1, -1 om
23	$CN + C \leftrightarrow C_2 + N$	3.000e+14	0.00	1.810e+04	T_{tr}	+1, -1 om
24	$CN + H_2 \leftrightarrow HCN + H$	2.95e+05	0.0	1.13e+03	T_{tr}	F=5.0
25	$CN + O \leftrightarrow NO + C$	1.600e+12	0.10	1.460e+04	T_{tr}	+1, -0 om
26	$CO + C \leftrightarrow C_2 + O$	2.40e+17	-1.00	5.800e+04	T_{tr}	+1, -1 om
27	$CO + C_2 \leftrightarrow C_3 + O$	1.000e+12	0.00	4.120e+04	T_{tr}	+1, -1 om
28	$CO + N \leftrightarrow CN + O$	1.000e+14	0.00	3.860e+04	T_{tr}	+1, -1 om
29	$CO + NO \leftrightarrow CO_2 + N$	3.0e+6	0.88	1.33e+4	T_{tr}	+1, -1 om
30	$CO + O \leftrightarrow O_2 + C$	3.900e+13	-0.18	6.920e+04	T_{tr}	+1, -0 om
31	$CO_2 + O \leftrightarrow O_2 + CO$	2.710e+14	0.0	3.3797e+04	T_{tr}	+1, -1 om
32	$H + C_2H_2 \leftrightarrow C_2H + H_2$	1.e+16	-0.5	1.55e+4	T_{tr}	+1, -1 om
33	$H + CN \leftrightarrow CH + N$	1.5e+15	-0.12	4.976e+4	T_{tr}	+1, -1 om
34	$H + CO \leftrightarrow CH + O$	6.7e+14	0.15	8.847e+4	T_{tr}	+1, -1 om
35	$H_2 + C \leftrightarrow CH + H$	4.00e+14	0.00	1.17e+04	T_{tr}	+1, -1 om
36	$H_2 + H \leftrightarrow 2H + H$	8.5e+19	-1.1	5.2335e+04	T_a	+1, -1 om
37	$N + CO \leftrightarrow NO + C$	1.1e+14	0.07	5.35e+4	T_{tr}	+1, -1 om
38	$N_2 + C \leftrightarrow CN + N$	1.100e+14	-0.11	2.320e+04	T_{tr}	+50, -50%
39	$N_2 + CO \leftrightarrow CN + NO$	1.2e+16	-1.23	7.70e+4	T_{tr}	+1, -1 om
40	$N_2 + O \leftrightarrow NO + N$	6.0e+13	0.1	3.800e+04	T_{tr}	+50, -50%
41	$O_2 + N \leftrightarrow NO + O$	2.49e+9	1.18	4.005e+03	T_{tr}	+1, -1 om

Table A3: Flow Field Ionization Reactions

#	Reaction	$A_{f,i}$	$n_{f,i}$	$D_{f,i}$	$T_{f,i}$	Uncertainty
42	$C + e^- \leftrightarrow C^+ + e^- + e^-$	5.05e+29	-3.00	1.3072e+05	T_{ve}	+1, -1 om
43	$C^+ + N_2 \leftrightarrow N_2^+ + C$	1.11e+14	-0.11	5.0000e+04	T_{tr}	+1, -1 om
44	$H + e^- \leftrightarrow H^+ + e^- + e^-$	2.20e+30	-2.80	1.5780e+05	T_{ve}	+1, -1 om
45	$N + N \leftrightarrow N_2^+ + e^-$	4.400e+07	1.50	6.750e+04	T_{ve}	+1, -1 om
46	$N + O \leftrightarrow NO^+ + e^-$	5.300e+12	0.00	3.190e+04	T_{ve}	+1, -1 om
47	$N + e^- \leftrightarrow N^+ + e^- + e^-$	2.50e+34	-3.82	1.682e+05	T_{ve}	+1, -1 om
48	$N^+ + N_2 \leftrightarrow N_2^+ + N$	1.000e+12	0.50	1.220e+04	T_{ve}	+1, -1 om
49	$N_2 + O^+ \leftrightarrow N_2^+ + O$	9.100e+11	0.36	2.280e+04	T_{tr}	+1, -1 om
50	$N_2 + e^- \leftrightarrow 2N + e^-$	6.0e+3	2.6	1.132e+5	T_{ve}	+1, -1 om
51	$NO + O^+ \leftrightarrow N^+ + O_2$	1.400e+05	1.90	2.660e+04	T_{tr}	+1, -1 om
52	$NO^+ + C \leftrightarrow C^+ + NO$	1.0e+13	0.0	2.32e+4	T_{tr}	+1, -1 om
53	$NO^+ + N \leftrightarrow N_2^+ + O$	7.200e+13	0.00	3.550e+04	T_{tr}	+1, -1 om
54	$NO^+ + N \leftrightarrow O^+ + N_2$	3.400e+13	-1.08	1.280e+04	T_{tr}	+1, -1 om
55	$NO^+ + O \leftrightarrow N^+ + O_2$	1.000e+12	0.50	7.720e+04	T_{tr}	+1, -1 om
56	$NO^+ + O \leftrightarrow O_2^+ + N$	7.200e+12	0.29	4.860e+04	T_{tr}	+1, -1 om
57	$NO^+ + O_2 \leftrightarrow NO + O_2^+$	2.400e+13	0.41	3.260e+04	T_{tr}	+1, -1 om
58	$O + O \leftrightarrow O_2^+ + e^-$	7.100e+02	2.70	8.060e+04	T_{ve}	+1, -1 om
59	$O + e^- \leftrightarrow O^+ + e^- + e^-$	3.900e+33	-3.78	1.585e+05	T_{ve}	+1, -1 om
60	$O_2 + C^+ \leftrightarrow O_2^+ + C$	1.0e+13	0.0	9.4e+3	T_{tr}	+1, -1 om
61	$O_2^+ + N \leftrightarrow O_2 + N^+$	8.700e+13	0.14	2.860e+04	T_{tr}	+1, -1 om
62	$O_2^+ + N_2 \leftrightarrow N_2^+ + O_2$	9.900e+12	0.00	4.070e+04	T_{tr}	+1, -1 om
63	$O_2^+ + O \leftrightarrow O^+ + O_2$	4.000e+12	-0.09	1.800e+04	T_{tr}	+1, -1 om
64	$O_2 + e^- \leftrightarrow O_2^+ + e^- + e^-$	2.19e+10	1.16	130102.0	T_{ve}	+1, -1 om

Table A4: Uncertain Molecular Band Processes

Molecule	Upper State – Lower State	Band Name	λ Range (nm)	Uncertainty
CO	$A^1\Pi - X^1\Sigma^+$	4th Positive	120 – 280	+/- 40%
CO	$X^1\Sigma^+ - X^1\Sigma^+$	Infrared	1200 – 7000	+/- 50%
CN	$A^2\Pi_i - X^2\Sigma^+$	Red	400 – 2800	+/- 30%
CN	$B^2\Sigma^+ - X^2\Sigma^+$	Violet	300 – 550	+/- 15%
C ₂	$d^3\Pi_g - a^3\Pi_u$	Swan	390 – 1000	+/- 50%
H ₂	$B^1\Sigma_u^+ - X^1\Sigma_g^+$	Lyman	120 – 170	+/- 10%
H ₂	$C^1\Pi_u - X^1\Sigma_g^+$	Werner		+/- 20%
N ₂		Carroll-Yoshino		+/- 50%
N ₂		First-Positive		+/- 10%
N ₂ ⁺		First-Negative		+/- 10%
N ₂		Second-Positive		+/- 10%
NO		Beta		+/- 50%
NO		Delta		+/- 50%
NO		Epsilon		+/- 50%

Table A5: Uncertain Atomic Nitrogen Lines

λ_{multi} (nm)	i	j	Wiese ID	$\pm f_{ij}$	$\pm \Delta\lambda_{S,O}$
120.00	1	4	1	20%	50%
149.33	2	5	15	10%	30%
174.36	3	5	29	20%	50%
745.22	4	10	48	10%	30%
821.41	4	9	47	10%	30%
869.40	4	8	46	15%	30%
1160.0	6	10	61	25%	100%
113.47	1	6	2	10%	50%
1353.0	5	7	50	10%	50%
1490.9	6	8	59	10%	100%
1355.1	6	9	60	25%	100%

Table A6: Uncertain Atomic Oxygen Lines

λ_{multi} (nm)	i	j	Wiese ID	$\pm f_{ij}$	$\pm \Delta\lambda_{S,O}$
130.35	1	5	2	3	50
844.88	5	7	60	10	50
777.55	4	6	56 0	3	50
104.01	1	9	6	25	50
135.60	1	4	1	25	50
164.13	2	5	4	25	50
172.71	2	4	3	25	50
232.54	3	5	5	25	50
672.80	4	7	57	25	50
1016.7	5	6	59	25	50
1128.7	7	11	78	25	50

Table A7: Uncertain Molecular Heavy-Particle Impact Excitation Rates (cm³/s) for non-Boltzmann Modeling

#	Reaction	A_{hp}	n_{hp}	E_{hp}	Uncertainty
1	$CN(X^2\Sigma^+) + M \leftrightarrow CN(A^2\Pi) + M$	M dependent			+/- 1 om
2	$CN(A^2\Pi) + M \leftrightarrow CN(B^2\Sigma^+) + M$	M dependent			+/- 1 om
3	$CN(B^2\Sigma^+) + M \leftrightarrow CN(a^4\Sigma^+) + M$	M dependent			+/- 2 om
4	$CN(a^4\Sigma^+) + M \leftrightarrow CN(D^2\Pi^+) + M$	M dependent			+/- 2 om
5	$CO(X^1\Sigma^+) + M \leftrightarrow CO(a^3\Pi) + M$	M dependent			+/- 1 om
6	$CO(X^1\Sigma^+) + M \leftrightarrow CO(a'^3\Sigma^+) + M$	5.20E-10	0.500	80370.0	+/- 1 om
7	$CO(X^1\Sigma^+) + M \leftrightarrow CO(d^3\Delta) + M$	2.61E-11	0.500	87975.0	+/- 1 om
8	$CO(X^1\Sigma^+) + M \leftrightarrow CO(A^1\Pi) + M$	2.52E-09	0.344	93669.0	+/- 1 om
9	$CO(a^3\Pi) + M \leftrightarrow CO(a'^3\Sigma^+) + M$	M dependent			+/- 2 om
10	$CO(a'^3\Sigma^+) + M \leftrightarrow CO(d^3\Delta) + M$	M dependent			+/- 2 om
11	$CO(d^3\Delta) + M \leftrightarrow CO(e^3\Sigma^-) + M$	M dependent			+/- 2 om
12	$CO(e^3\Sigma^-) + M \leftrightarrow CO(A^1\Pi) + M$	8.78e-11	0.498	971.0	+/- 2 om

Table A8: Uncertain Molecular Electron-Impact Excitation Rates (cm³/s) for non-Boltzmann Modeling

#	Reaction	A_{el}	n_{el}	E_{el}	Uncertainty
1	$\text{CN}(X^2\Sigma^+) + e^- \leftrightarrow \text{CN}(A^2\Pi) + e^-$	6.41e-09	0.20	18303	+/- 1 om
2	$\text{CN}(X^2\Sigma^+) + e^- \leftrightarrow \text{CN}(B^2\Sigma^+) + e^-$	6.83e-10	0.39	40428	+/- 1 om
3	$\text{CN}(X^2\Sigma^+) + e^- \leftrightarrow \text{CN}(a^4\Sigma^+) + e^-$	5.13e-11	0.35	47323	+/- 2 om
4	$\text{CN}(X^2\Sigma^+) + e^- \leftrightarrow \text{CN}(D^2\Pi^+) + e^-$	4.07e-10	0.25	79368	+/- 2 om
5	$\text{CN}(A^2\Pi) + e^- \leftrightarrow \text{CN}(B^2\Sigma^+) + e^-$	1.36e-04	-0.74	28030	+/- 2 om
6	$\text{CN}(A^2\Pi) + e^- \leftrightarrow \text{CN}(a^4\Sigma^+) + e^-$	4.55e-04	-0.77	37548	+/- 2 om
7	$\text{CN}(A^2\Pi) + e^- \leftrightarrow \text{CN}(D^2\Pi^+) + e^-$	1.22e-03	-0.82	69300	+/- 2 om
8	$\text{CN}(B^2\Sigma^+) + e^- \leftrightarrow \text{CN}(a^4\Sigma^+) + e^-$	7.85e-05	-0.66	14148	+/- 2 om
9	$\text{CN}(B^2\Sigma^+) + e^- \leftrightarrow \text{CN}(D^2\Pi^+) + e^-$	6.29e-04	-0.79	45559	+/- 2 om
10	$\text{CN}(a^4\Sigma^+) + e^- \leftrightarrow \text{CN}(D^2\Pi^+) + e^-$	4.23e-04	-0.77	36015	+/- 2 om
11	$\text{CO}(X^1\Sigma^+) + e^- \leftrightarrow \text{CO}(a^3\Pi) + e^-$	8.42e-11	0.28	80530	+/- 1 om
12	$\text{CO}(X^1\Sigma^+) + e^- \leftrightarrow \text{CO}(a^3\Sigma^+) + e^-$	1.82e-14	1.17	102434	+/- 1 om
13	$\text{CO}(X^1\Sigma^+) + e^- \leftrightarrow \text{CO}(d^3\Delta) + e^-$	3.16e-12	0.66	114626	+/- 1 om
14	$\text{CO}(X^1\Sigma^+) + e^- \leftrightarrow \text{CO}(e^3\Sigma^-) + e^-$	2.10e-14	1.17	113995	+/- 1 om
15	$\text{CO}(X^1\Sigma^+) + e^- \leftrightarrow \text{CO}(A^1\Pi) + e^-$	3.82e-09	0.12	95850	+/- 1 om
16	$\text{CO}(a^3\Pi) + e^- \leftrightarrow \text{CO}(a^3\Sigma^+) + e^-$	4.43e-8	-0.73	23456	+/- 1 om
17	$\text{CO}(a^3\Pi) + e^- \leftrightarrow \text{CO}(d^3\Delta) + e^-$	7.74e-15	1.17	44552	+/- 1 om
18	$\text{CO}(a^3\Pi) + e^- \leftrightarrow \text{CO}(e^3\Sigma^-) + e^-$	3.21e-15	1.27	44896	+/- 1 om
19	$\text{CO}(a^3\Pi) + e^- \leftrightarrow \text{CO}(A^1\Pi) + e^-$	1.49e-05	-0.74	27860	+/- 2 om
20	$\text{CO}(a^3\Sigma^+) + e^- \leftrightarrow \text{CO}(d^3\Delta) + e^-$	2.53e-11	0.16	10611	+/- 1 om
21	$\text{CO}(a^3\Sigma^+) + e^- \leftrightarrow \text{CO}(e^3\Sigma^-) + e^-$	6.04e-13	0.61	11041	+/- 1 om
22	$\text{CO}(a^3\Sigma^+) + e^- \leftrightarrow \text{CO}(A^1\Pi) + e^-$	6.56e-06	-0.69	17750	+/- 2 om
23	$\text{CO}(d^3\Delta) + e^- \leftrightarrow \text{CO}(e^3\Sigma^-) + e^-$	1.09e-10	1.66	10686	+/- 1 om
24	$\text{CO}(d^3\Delta) + e^- \leftrightarrow \text{CO}(A^1\Pi) + e^-$	2.62e-06	-0.63	10570	+/- 2 om
25	$\text{CO}(e^3\Sigma^-) + e^- \leftrightarrow \text{CO}(A^1\Pi) + e^-$	1.41e-06	-0.58	6971	+/- 2 om